Estimation of Wind-Induced Error of Rainfall Gauge Measurements Using a Numerical Simulation

VLADISLAV NEŠPOR AND BORIS SEVRUK

Department of Geography, Swiss Federal Institute of Technology ETH, Zurich, Switzerland

(Manuscript received 12 December 1997, in final form 28 May 1998)

ABSTRACT

A new method of estimating the wind-induced error of rainfall gauge measurements is presented. The method is based on a three-dimensional numerical simulation of the airflow around a precipitation gauge and subsequent computation of particle trajectories. Three-dimensional velocity and turbulence flow fields around a gauge are computed for wind speeds ranging between 1 and 12 m s^{-1} by employing the k–ε turbulence model. Two-dimensional measurements of the flow using a constant temperature anemometer are carried out in a wind tunnel. The measurement results are used to verify numerical flow simulations. Subsequently, the computed flow fields are used for raindrop trajectory simulations and assessment of wind-induced measurement errors related to a given unique drop diameter and wind speed. These errors are approximated by a gamma-type function and integrated over a gamma drop size distribution. The resulting wind-induced error is presented as a function of the rate of rainfall, wind speed, and drop size distribution parameters. The wind-induced measurement error is evaluated for three operational precipitation gauges. The results show an increase of the error with a decreasing rainfall rate, and increasing wind speed and fraction of smaller drops. The comparison of gauges also reveals differences. The computed wind-induced errors are compared with the errors derived from field rainfall measurements. The compared values show a relatively good agreement.

1. Introduction

The knowledge of the amount and distribution of precipitation with respect to time and space is an essential element of water and energy balance studies, and is an important input into runoff computations, flood forecasting, and various engineering design computations. Precipitation data can be obtained by different means. The oldest and the most common method is in situ measurement using can-type precipitation gauges. Other methods based on modern remote sensing techniques by radars and satellites have to be calibrated against the gauge measurement (e.g., Sevruk 1989a).

Unfortunately, measurements by precipitation gauges also suffer from inaccuracies and are subject to random and systematic errors. The basic sources of the systematic error of the gauge are the deviation of precipitation particle trajectories due to wind field deformation around the gauge, wetting of inner walls of the gauge, and evaporation of the water accumulated in the gauge container. The wind-induced error, which can be on average 2%–10% for rain and 10%–50% for snow (e.g., Sevruk 1985), is the most important component of systematic error.

There are three basic possibilities of estimating the wind-induced error of precipitation gauges: 1) field intercomparisons, 2) wind tunnel measurements, and 3) numerical simulations. The advantage of field intercomparisons is that precipitation gauges are installed in the operational position and exposed to meteorological conditions with their natural variability. The collected amount of precipitation is then compared to some reference measurement. In the case of rain, the reference measurements are made by a pit gauge (Sevruk and Hamon 1984), and in the case of snow, by the Double Fence Intercomparison Reference (DFIR) (Yang et al. 1994).

A significant disadvantage of field experiments is the long period of observation necessary to obtain a sufficient dataset. Moreover, a better understanding of the relationship between the wind-induced error and the influencing meteorological variables requires their measurement at high temporal resolution. This is usually associated with added complexity and cost of experiments.

The advantage of wind tunnel measurements is that the process around a precipitation gauge can be investigated in controlled laboratory conditions. The information about velocity and turbulence fields above the gauge, resulting from measurements, can be further used

Corresponding author address: Dr. Vladislav Nešpor, Department of Geography, Swiss Federal Institute of Technology ETH, Winterthurerstr. 190, 8057 Zurich, Switzerland.
E-mail: nespor@geo.umnw.ethz.ch

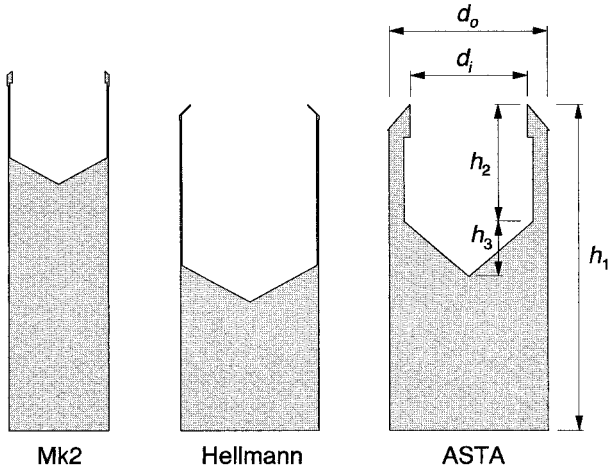

FIG. 1. Schematic vertical cross sections of the investigated precipitation gauges. The relative size proportions are preserved. The corresponding dimensions are in Table 1.

for the computation of precipitation particle trajectories (e.g., Folland 1988). Another possibility is to replace real precipitation particles by artificial ones and to estimate the wind-induced error by direct measurement of the collecting efficiency of the gauge (e.g., Hall et al. 1993).

However, the wind tunnel measurements are not free of difficulties. Detailed measurement of velocity vector fields, necessary for particle trajectory computation, is a rather complicated process requiring sophisticated and expensive equipment. In the case of artificial particles, the difficulty is that for realistic results the particles should mimic properties of free-falling precipitation, which is not easy to achieve.

The process of the wind-induced error assessment can be accelerated significantly by numerical simulations. Similar to wind tunnel measurements, there are two possibilities. The gauge error can be estimated either from a computation of the two-phase flow (Carlsson and Svensson 1984) or from a separate computation of the airflow and, subsequently, the precipitation particle movement. In contrast to measurements, the flow simulation on computers gives complex and detailed information about the flow field in a more convenient, faster, and less expensive way. There is also the possibility of easily changing, for example, properties of the air, important shape parameters of the gauge, and other boundary conditions, and of investigating their influence on the wind-induced error.

But numerical simulations also have limitations. Generally, the validity of the results depends on simplifications made in the physical description of the processes leading to the wind-induced error as well as on the precision of the procedures used. Therefore, results from numerical simulation should still be verified by measurements.

The main goals of the work presented here were to investigate the physical process around a precipitation gauge leading to the wind-induced error of measurement and to develop a procedure for a more convenient assessment of this error. The investigations were concentrated on three operational precipitation gauges: the British Meteorological Office Mk2 gauge, and the Hellmann gauge and the ASTA (automatic station tipping bucket) gauge used in Switzerland. In operation, the Mk2 gauge is positioned on the ground, and the Hellmann and ASTA gauges are elevated, usually between 1.5 and 2 m above ground. The investigated gauges differ in the orifice diameter, the height and diameter of the body, and other shape parameters. The schematic vertical cross sections of the gauges are shown in Fig. 1, and the basic dimensions are summarized in Table 1.

TABLE 1. Basic dimensions of the investigated precipitation gauges according to Fig. 1.

	Dimensions [mm]				
Gauge	d_i	d_o	h_1	h_2	h_3
Mk2	127	136.6	490	118	36
Hellmann	160	188	445	220	50
ASTA	160	216	445	160	75

2. Methods

Usually, precipitation particles have relatively low numbers (densities) per unit volume of the air. Therefore, it can be assumed that the particulate phase does not influence the continuous phase (the air), so these two phases can be simulated separately. Moreover, for small domains with volumes of a few cubic meters, the interference of particles can be neglected, and each particle can be regarded as being alone in the flow.

In the present assessment of the wind-induced error, we selected three-dimensional numerical simulations of the flow and particle movement as the basic approach. The error assessment included several steps. First, we measured the flow around a precipitation gauge in a wind tunnel. Then, we simulated the flow numerically, and the measured data were used to verify the computational results. Subsequently, we used the computed flow fields for raindrop trajectory simulations and assessment of the error associated with a given unique drop diameter and wind speed. Finally, this error was integrated over a drop size distribution.

Details of the measurements and numerical simulations described here can be found in Nešpor (1996). The computations were made for the meteorological conditions and properties of the air summarized in Table 2.

TABLE 2. Meteorological conditions (the temperature T, pressure p, and relative humidity r) and the corresponding density ρ_a and kinematic viscosity ν_a of the air used in the present computations.

T [°C]	p [kPa]	r [%]	ρ_a [kg m^{-3}]	ν_a [m^2 s^{-1}]
20	101.325	80	1.204	1.510×10^{-5}

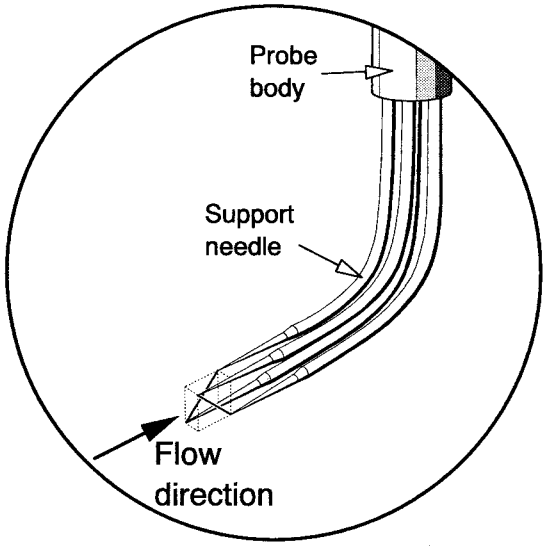

FIG. 2. A detail of the TSI boundary layer X probe used for two velocity component measurements of the flow above a precipitation gauge. The probe sensors are perpendicular and formed by tungsten wires.

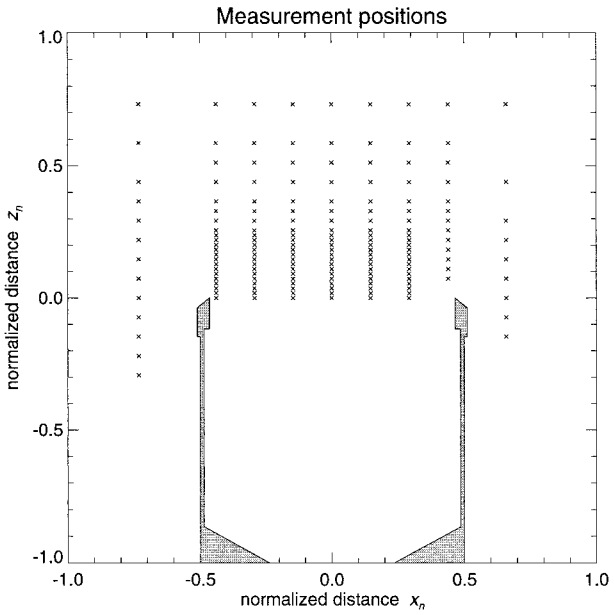

FIG. 3. Distribution of the measurement positions above the Mk2 gauge. The distances were normalized by the outer gauge diameter. The direction of the measured flow was from left to right.

a. Wind flow measurements

Wind flow measurements served the purpose of studying the basic characteristics of the flow around the Mk2 precipitation gauge and of providing reference data for the verification of numerical flow simulation. The wind tunnel used for measurements was of the nonrecirculating suction type. The cross section (width × height) of the tunnel test section was 1.2 m × 1.4 m.

The turbulence intensity, often used in connection with turbulence measurements as a characteristic of the flow, is defined as (e.g., Hinze 1975; Lomas 1986)

$$I = \frac{v'_m}{\overline{v_m}}, \tag{1}$$

where v'_m is the root mean square (rms) value of velocity magnitude fluctuations and $\overline{v_m}$ is the mean velocity. During the measurements in the wind tunnel, the air velocity at the gauge orifice was set to approximately 3 m s^{-1}, and the free-stream turbulence intensity without the presence of the gauge was very low, that is, approximately 0.01.

We carried out two-dimensional measurements of horizontal and vertical velocity vector components and turbulence characteristics using a constant temperature anemometer equipped with the TSI[1] boundary layer X probe. The X probe, shown in Fig. 2, was formed by two perpendicular tungsten wire sensors. The active sensing length was 1.25 mm, and the spacing between the sensors was 1 mm.

[1] TSI Incorporated, 500 Cardigan Road, P.O. Box 64394, St. Paul, MN 55164.

Figure 3 depicts the measurement positions in profiles in front of and above the gauge in the plane of symmetry—the vertical plane parallel to the flow—and going through the center of the gauge. The measurement area extended 0.18 m above the gauge, and 0.16 m upstream and 0.09 m downstream from the gauge center. The vertical distance between measurement positions in profiles was 2.5 mm in the region close to the gauge orifice, and the horizontal distance between the profiles was 20 mm above the gauge. During the measurement, in each position the probe was aligned to the mean velocity vector by rotation of the probe around the horizontal cross-flow axis.

The flow around the gauge is divided into the internal recirculating flow inside the gauge collector and the external main flow around the gauge. These two flows are separated by a thin shear layer above the gauge opening. The measurement results in Fig. 4 show the basic characteristics of the airflow in the plane of symmetry. Because of the blocking effect of the gauge, the external airflow is deviated around the gauge and accelerated. Wind velocities above the gauge orifice are approximately 35% higher than the free-stream velocity, and the strongest production of turbulence above the gauge is in the shear layer along the separation between the internal and external flows.

b. Wind flow computations

The aim of wind flow computations was to provide a fully three-dimensional description of the flow around precipitation gauges suitable for the subsequent simulation of particle movement. For the flow computations

we used PHOENICS (version 2.0), a general flow simulation software developed by Concentration Heat and Momentum Ltd. (CHAM).[2] The discretization method employed in PHOENICS is based on the control-volume formulation.

To adequately represent the shape of the investigated precipitation gauge, we selected the cylindrical coordinate system. The vertical z axis was set to be identical to the central axis of the gauge. We assumed the flow around the gauge to be symmetrical about the vertical plane of symmetry. The extent of the half-cylindrical computational domain was 3.5 times the outer diameter of the gauge above the gauge orifice and 2.75 times the outer diameter to each side of the gauge body. The final discretization of the computational domain varied slightly from gauge to gauge. The largest number of grid cells was 40 in the angular, 65 in the radial, and 120 in the vertical directions. The solid gauge body was represented by totally blocking selected cell faces and cell volumes inside the computational domain. The domain discretization was finer above the gauge orifice and close to the gauge body.

For the flow computation, we selected the k–ε turbulence model with the standard values of coefficients (Launder and Spalding 1974). The inflow boundary condition was specified at the windward half of the cylindrical surface of the computational domain. At the inflow surface, the pressure was fixed to zero, and we assumed a simplified vertical free-stream velocity profile with a velocity magnitude constant with height. The turbulence variables were also assumed to be constant with height at the inflow. Their values were derived from the turbulence intensity I and the turbulent kinematic viscosity

$$\nu_t = C_\mu \frac{k^2}{\varepsilon}, \tag{2}$$

where $C_\mu = 0.09$ is the coefficient in the standard k–ε turbulence model (Launder and Spalding 1974). To be close to the conditions in the wind tunnel, we had chosen $I = 0.03$ and $\nu_t = \nu_a$, where ν_a is the kinematic viscosity of the air (Table 2).

The original PHOENICS code did not prove to be very accurate for computations in the cylindrical coordinate system. The first solution of the flow above the Mk2 precipitation gauge using the k–ε turbulence model showed an imprecise computation of the turbulence quantities at the plane of symmetry and near the central axis of the gauge. The problem was most severe in the shear layer above the gauge at the central axis, where the production of turbulence was strongly overestimated (Nešpor 1996). A detailed analysis of the results revealed that the imprecise computation of the turbulence quantities was caused mainly by inaccurate evaluation of the partial derivatives of velocity components in the cylindrical coordinates. Fortunately, it is possible to access parts of the PHOENICS code, and we were able to replace the incorrect subroutines with a new FORTRAN code and to improve the precision of computation.

We computed the flow around the Mk2, Hellmann, and ASTA gauges for the free-stream velocity of the air v_f between 1 and 12 m s^{-1}. The direct comparison of normalized values of velocity components, turbulent kinetic energy, and its dissipation rate did not show very large differences between the gauges. Compared with the Mk2 and Hellmann gauges, the turbulence production and the relative increase of velocity magnitude above the gauge orifice were slightly higher in the case of the ASTA precipitation gauge. The main difference between the investigated gauges was in the absolute extent of the disturbed space around the gauge, but this is the natural consequence of the differences in size of the gauge bodies (see Table 1).

Figure 5 shows an example of results for the Mk2 gauge and $v_f = 3$ m s^{-1}. The comparison of the computed flow fields with measurement results shows good agreement (see Figs. 4 and 5). Compared with measurements, the numerical simulation predicts slightly larger values of velocity magnitude and turbulence quantities above the gauge orifice. In spite of that, the flow fields resulting from numerical simulation are suitable for computation of precipitation particle trajectories.

c. Particle trajectory computations

In the present computations, we used the Lagrangian formulation describing the flow of a number of discrete particles by tracking them one by one. The linear momentum equation for a single particle moving in the air is (see, e.g., Hinze 1975; Narasimhamurty et al. 1986; Astrup 1992)

$$V_p \rho_p \mathbf{a}_p = \int_S \mathbf{n}_S \sigma_p \, dS + V_p(\rho_p - \rho_a)\mathbf{g}, \tag{3}$$

where V_p is the particle volume; ρ_a and ρ_p are the densities of the air and the particle, respectively; $\mathbf{a}_p = (a_x, a_y, a_z)$ is the particle acceleration vector; $\mathbf{n}_S$ is the outward unit vector normal to the particle surface S; σ_p is the stress tensor; and $\mathbf{g}$ is the acceleration vector due to gravity.

The surface stress integral on the right-hand side of (3) represents the total force acting on the particle surface. This force can be decomposed into partial forces for different situations. According to Hinze (1975), for slow motion of a spherical particle in the fluid, only the Stokes drag force becomes important, and other partial forces acting on the particle surface can be neglected, if the density of the particle is comparable to or higher

[2] Concentration Heat and Momentum Ltd., Bakery House, 40 High Street, Wimbledon Village, London SW19 5AU, United Kingdom.

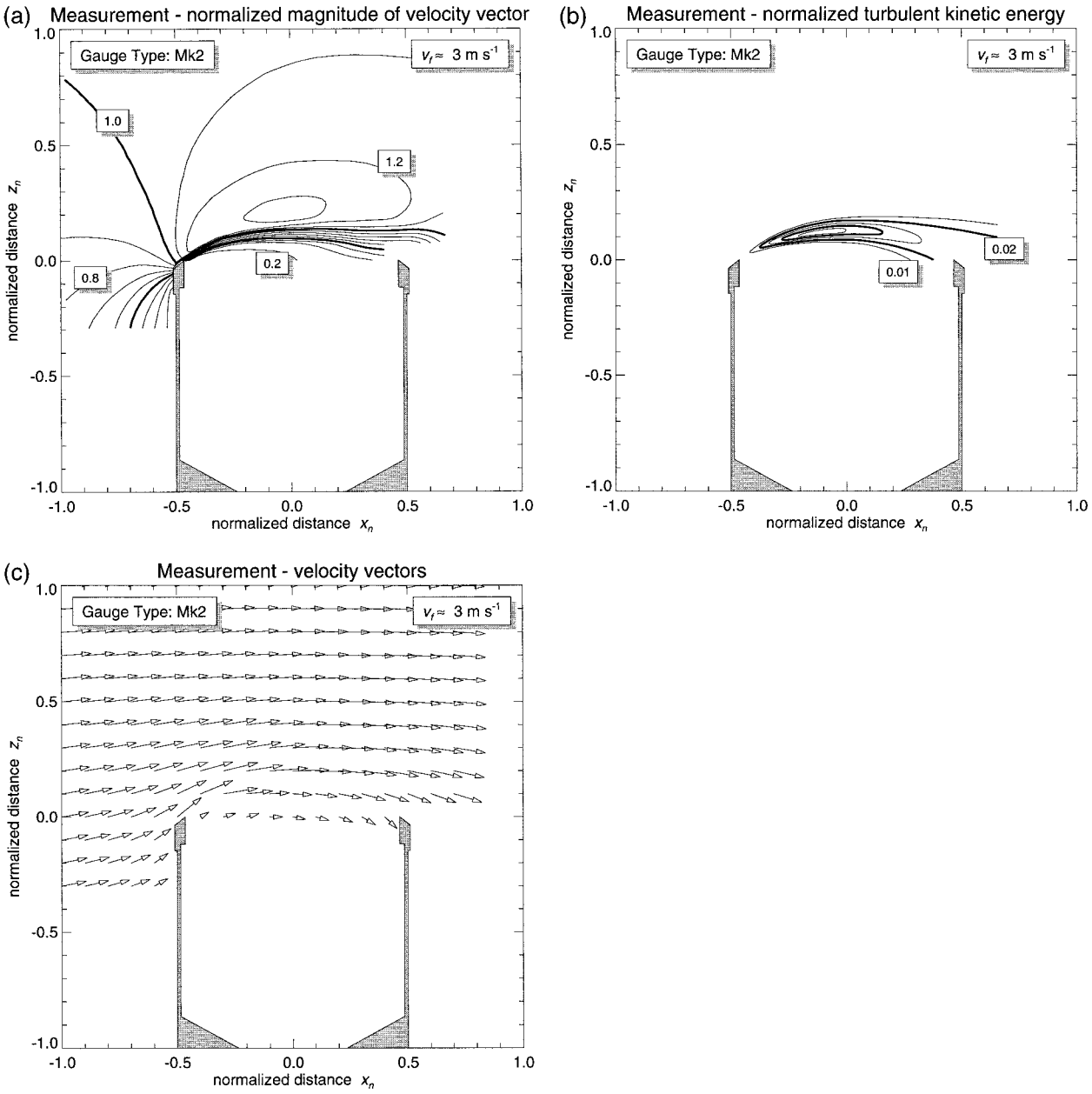

FIG. 4. Results of the measurement of the airflow above the Mk2 precipitation gauge. The free-stream velocity was $v_f \approx 3$ m s^{-1}. Contour lines of (a) normalized magnitude of velocity vector, (b) normalized turbulent kinetic energy, and (c) velocity vectors are plotted in the plane of symmetry. The distances were normalized by the outer gauge diameter d_o (see Fig. 1 and Table 1), the velocity values by v_f, and the values of turbulent kinetic energy by v_f^2. The direction of the flow is from left to right.

than the density of the fluid. If the positive orientation of the z axis is upward and values of the velocity and acceleration components are considered positive in the positive directions of the axes, from (3), the particle acceleration a_z can be expressed as

$$a_z = \frac{\rho_p - \rho_a}{\rho_p} g - \frac{1}{2} C_d \frac{A_f}{V_p} \frac{\rho_a}{\rho_p} (w_p - w_a)|\mathbf{v}_p - \mathbf{v}_a|, \quad (4)$$

where C_d is the particle drag coefficient, A_f is the particle frontal area, $g = -9.81$ m s^{-2} is the acceleration due to gravity, and w_p and w_a are the vertical velocity components of the particle and the air, respectively.

In the above equation, $\mathbf{v}_p - \mathbf{v}_a$ is the relative particle-to-air velocity with the norm (the magnitude of the velocity vector)

$$|\mathbf{v}_p - \mathbf{v}_a| = [(u_p - u_a)^2 + (v_p - v_a)^2 + (w_p - w_a)^2]^{1/2}. \quad (5)$$

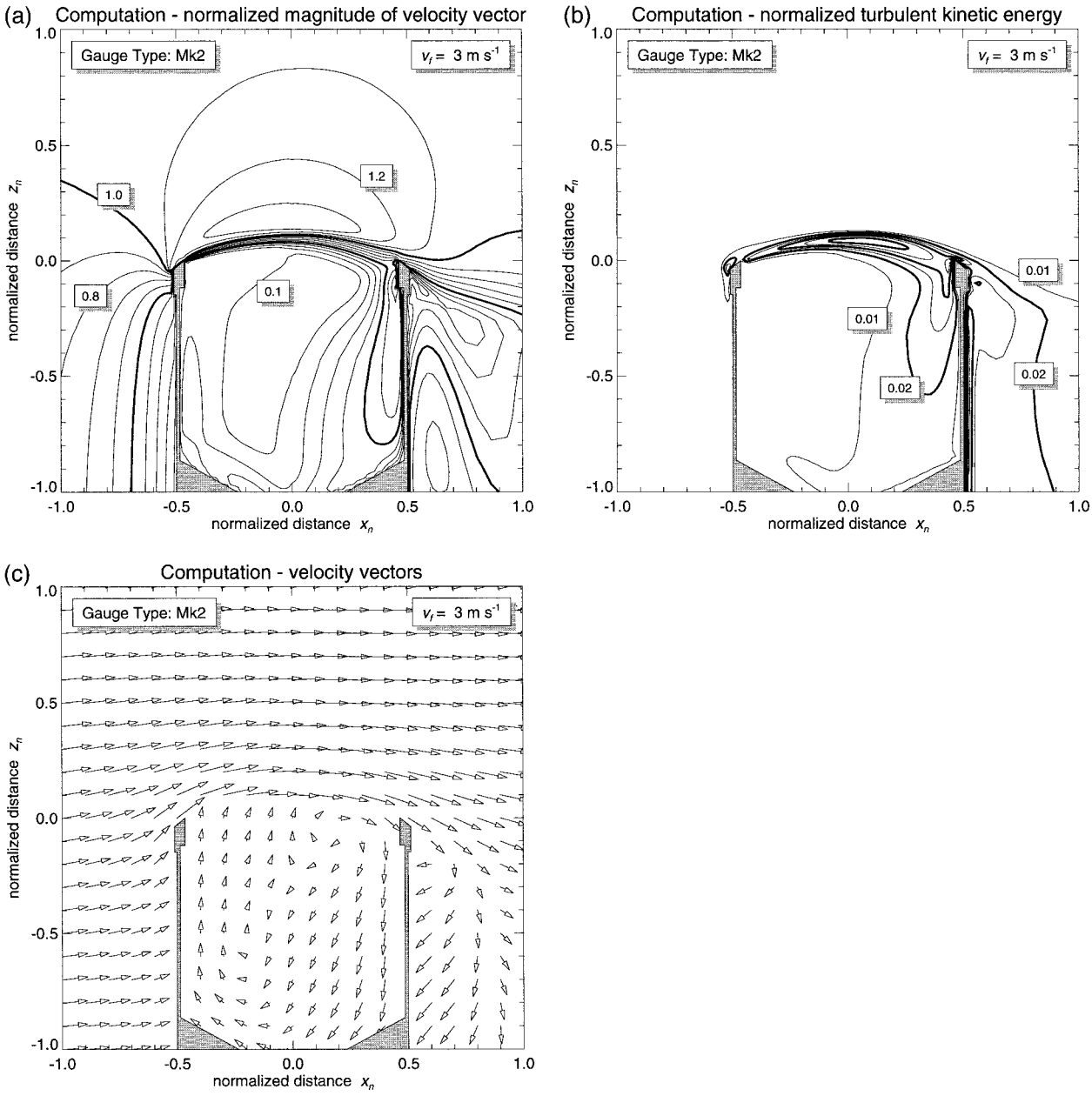

FIG. 5. The same as Fig. 4 but for computational results.

Similarly, the particle accelerations a_x and a_y in the horizontal x and y directions are

$$a_x = -\frac{1}{2}C_d\frac{A_f}{V_p}\frac{\rho_a}{\rho_p}(u_p - u_a)|\mathbf{v}_p - \mathbf{v}_a|, \tag{6}$$

$$a_y = -\frac{1}{2}C_d\frac{A_f}{V_p}\frac{\rho_a}{\rho_p}(v_p - v_a)|\mathbf{v}_p - \mathbf{v}_a|, \tag{7}$$

where u_p, u_a and v_p, v_a are the velocity components of the particle and the air, corresponding to the horizontal directions x and y, respectively.

The particle drag coefficient C_d depends mainly on the flow regime around the particle (Beard 1976) characterized by the particle Reynolds number

$$\mathrm{Re}_p = \frac{D|\mathbf{v}_p - \mathbf{v}_a|}{\nu_a}, \tag{8}$$

where ν_a is the laminar kinematic viscosity of the air and D is the characteristic particle diameter. In the case of raindrops, D is the equivolume spherical diameter: the diameter of a sphere with the same volume as the drop.

In stagnant air, when the particle reaches its terminal

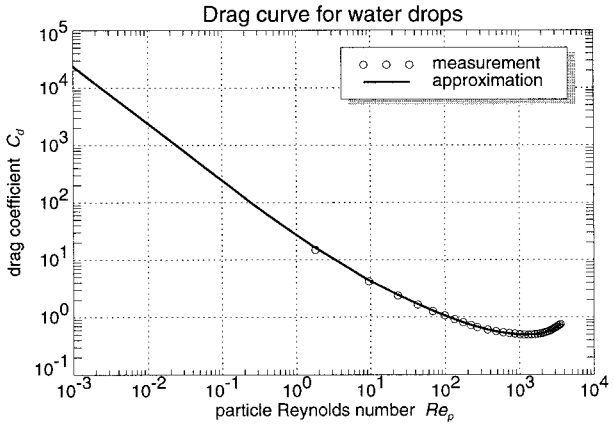

FIG. 6. The drag curve for water drops falling in stagnant air. The circles represent the measurement by Gunn and Kinzer (1949), and the solid line represents the approximation using formulas of Beard (1977). The properties of the air are summarized in Table 2.

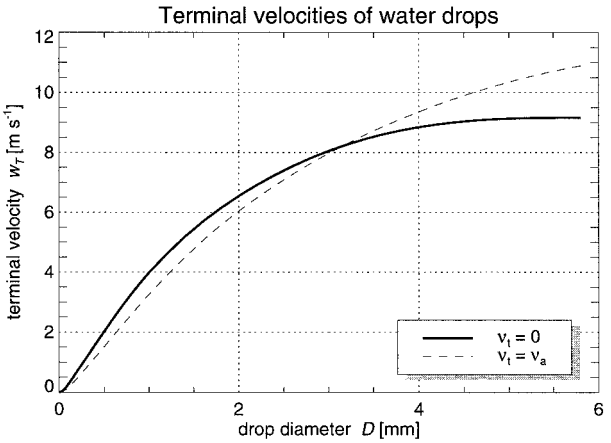

FIG. 7. Terminal velocities of water drops for the case without turbulence (solid line) and the case with turbulence (dashed line). Terminal velocity modifications were iteratively computed using (9) and (11) for $\nu_t = \nu_a$. For the properties of the air, see Table 2.

velocity w_T, the acceleration a_z is zero, and from (4), the particle drag coefficient is

$$C_d = 2\frac{\rho_p - \rho_a}{\rho_a} g \frac{V_p}{A_f} \frac{1}{w_T|w_T|}, \tag{9}$$

and the corresponding Reynolds number from (8) is

$$\mathrm{Re}_p = \frac{D|w_T|}{\nu_a}. \tag{10}$$

The drag coefficient can be determined for any flow situation from the known Reynolds number. The dependence of C_d on Re_p is called ''drag curve.'' It can be derived from known terminal velocities and properties of the air for any type of precipitation particle (raindrops, snowflakes, etc.).

There are many different empirical formulas for an approximation of the drag curve and terminal velocities of precipitation particles. Beard (1977) developed approximation formulas for the determination of terminal velocities of water drops covering different meteorological conditions. Those formulas agree well with measurements of drop terminal velocities by Gunn and Kinzer (1949), and they were used in the present computations of raindrop trajectories. Figure 6 shows the drag curve for water drops.

First estimates of wind-induced errors were obtained by computing drop trajectories using drag coefficients based on the terminal velocities measured in stagnant air (Gunn and Kinzer 1949). These estimates were unrealistically low, approximately three to four times lower than expected wind-induced errors (Nešpor 1996). It seemed that additional production of turbulence in the shear layer above the gauge could play an important role.

According to Hinze (1975), the behavior of a discrete particle in a turbulent flow depends on the size of the particle with respect to the scale of turbulence of the fluid. If the particle is large compared with the smallest scale of turbulence—that is, the Kolmogorov scale—the major effect of the turbulence on the particle motion will be to increase its drag, and the particle will tend to follow the low-frequency movement of the turbulent flow. If the particle is very small compared with the smallest scale of turbulence, it will tend to follow all turbulent fluctuations. Results of the flow computations indicated that the Kolmogorov scale of turbulence in the region above and inside the gauge is less than 0.2 mm (Nešpor 1996). Usually, precipitation particles are larger than this value, and therefore, we can assume that the influence of turbulence on the particle movement is only to change the drag coefficient.

In the present computations we simplified the influence of turbulence. The aim was to take qualitatively into account the relatively increased turbulence in the shear layer above the gauge orifice compared with the turbulence in the free flow of the computed flow fields. The change of the drag coefficient was evaluated from the particle Reynolds number modified by replacing ν_a in (8) with the sum of the laminar and the turbulent kinematic viscosities. Thus, the new particle Reynolds number is

$$\mathrm{Re}_p = \frac{D|\mathbf{v}_p - \mathbf{v}_a|}{\nu_a + \nu_t}, \tag{11}$$

where ν_t is the turbulent kinematic viscosity evaluated from the computed flow fields using (2).

Particle terminal velocities also depend on the turbulence level present in the air (Stout et al. 1995). We used the above simplified approach to recompute the terminal velocities of water drops for the free-stream turbulence of computed flow fields. As mentioned in section 2b, the free-stream turbulence of computed flow fields is characterized by $\nu_t = \nu_a$. Figure 7 shows that, compared with stagnant air, the resulting terminal ve-

locities are lower for smaller drop diameters and higher for larger ones. The increase of terminal velocities for large drop diameters does not seem to be realistic, but it has practically no influence on the present computations, as the contribution of larger drops to the wind-induced error is negligible. It is necessary to note that the application of (11) is restricted to the present numerical simulations and that it is not suitable for an adjustment of terminal velocities in the boundary layer of the atmosphere, where the turbulence level is much higher than in the computed flow fields.

For a given particle diameter D and free-stream velocity v_f, the trajectory can be determined by computing changes in the particle position in an iterative manner. In each step, the changes between the starting and ending particle positions are

$$\Delta x = x_2 - x_1 = \left(u_{p1} + \frac{1}{2}a_x\Delta t\right)\Delta t,$$

$$\Delta y = y_2 - y_1 = \left(v_{p1} + \frac{1}{2}a_y\Delta t\right)\Delta t,$$

$$\Delta z = z_2 - z_1 = \left(w_{p1} + \frac{1}{2}a_z\Delta t\right)\Delta t, \qquad (12)$$

and the changes in the particle velocity are

$$\Delta u_p = u_{p2} - u_{p1} = a_x\Delta t,$$

$$\Delta v_p = v_{p2} - v_{p1} = a_y\Delta t,$$

$$\Delta w_p = w_{p2} - w_{p1} = a_z\Delta t. \qquad (13)$$

In the above equations, Δt is the time step and subscripts 1 and 2 denote the quantities in the starting and ending particle positions, respectively. The determination of C_d from Re_p and the subsequent computation of a_x, a_y, and a_z are based on the particle-to-air velocity difference $\mathbf{v}_p - \mathbf{v}_a$ and on the turbulent kinematic viscosity ν_t corresponding to the time step Δt. In the present computations, these quantities were evaluated as averages between the values at the starting and ending drop positions. Because in each step the evaluation of the drop accelerations involves quantities in the unknown ending position, an iterative computation had to be used. For example, the vertical air velocity component was evaluated as

$$w_{a,i+1} = \frac{1}{2}(w_{a1} + w_{a2,i}), \qquad (14)$$

where i is the iteration number and w_{a1} and $w_{a2,i}$ are vertical velocities of the air in the starting and ending particle positions, respectively. The iteration started for $w_{a2,0} = w_{a1}$ and continued until the desired precision of the ending drop position was reached.

d. Estimation of the partial wind-induced error

We use the term ''partial wind-induced error'' of the gauge for the error estimated from a fictive precipitation formed by particles of a given unique diameter and for a given free-stream velocity. This error is given as a relative number, and it can be expressed as the difference between unity and partial efficiency of the gauge. The partial efficiency can be regarded as the ratio of the number of precipitation particles of the unique diameter actually crossing the gauge orifice to the number of particles that would cross the same area defined by the orifice, without the disturbing presence of the gauge. Therefore, for a given gauge and properties of the air, the partial error is a function of the free-stream velocity and the precipitation particle diameter.

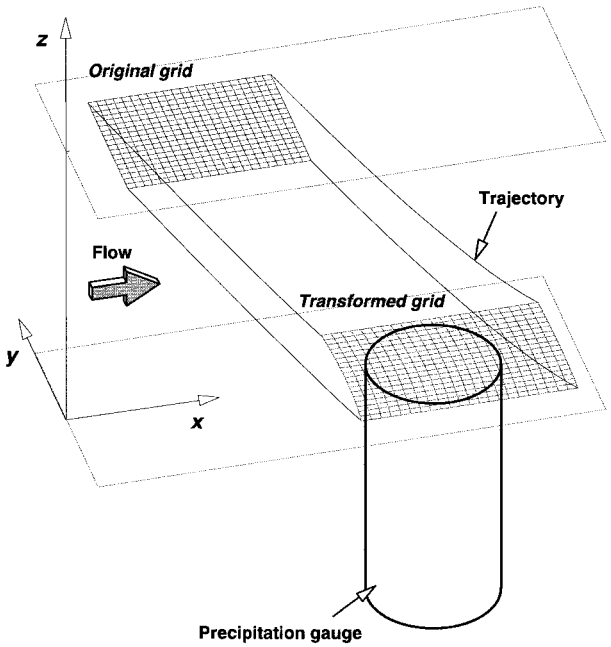

FIG. 8. A schematic plot of the transformation of the original grid in the undisturbed flow above the gauge to the transformed grid at the orifice height via particle trajectory computations for a given drop diameter and wind velocity.

In the present computations, we estimated the partial wind-induced error e_p by computing the transformation of a horizontal rectangular uniform grid from the undisturbed flow above the gauge to the horizontal plane at the height of the orifice, as illustrated in Fig. 8. The original horizontal grid in the undisturbed flow above the gauge can be understood as a representation of a fictive precipitation formed by drops of the unique diameter D uniformly distributed in the nodal points of the grid. For a given drop diameter D and free-stream velocity v_f, the transformation was determined by drop trajectories computed from each node of the original grid. Because some small drops had complicated trajectories passing the horizontal plane at the height of the gauge orifice more than once, only the last intersection of the trajectory with this plane was recorded as a nodal point of the transformed grid.

The transformed grid can be seen as a representation of the drop distribution at the orifice height. If we as-

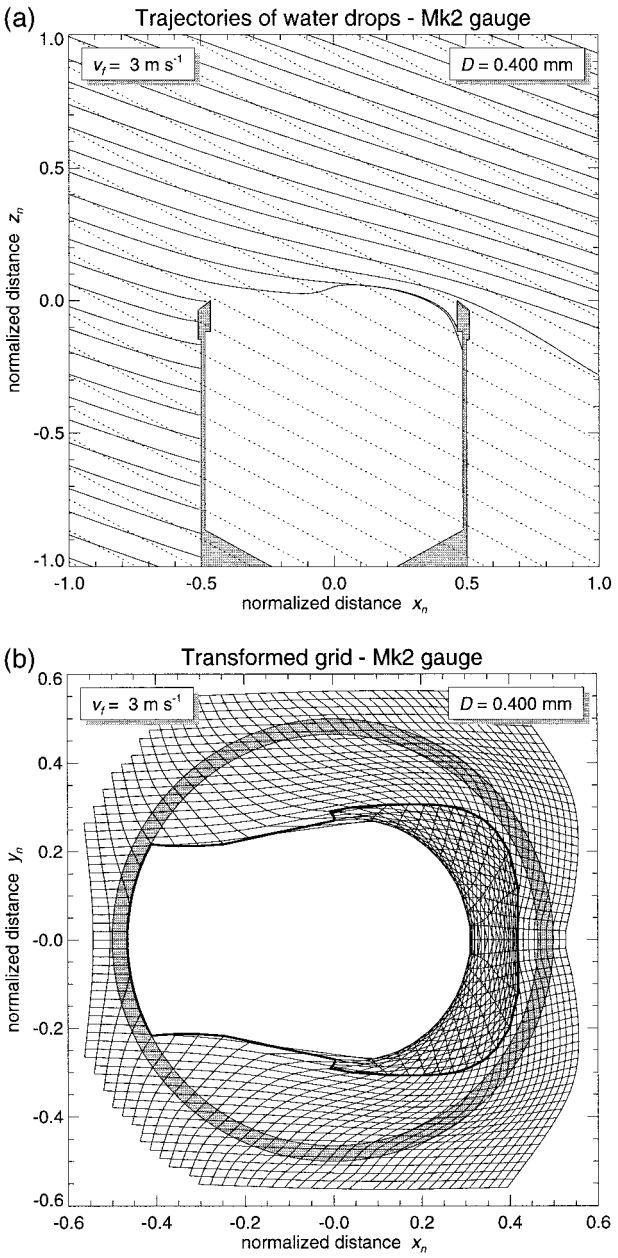

FIG. 9. An example of (a) computed trajectories of water drops in the vertical plane of symmetry and (b) the transformed grid in the horizontal plane at the height of the gauge orifice. The computation was made for the Mk2 gauge, free-stream velocity $v_f = 3$ m s^{-1}, and drop diameter $D = 0.4$ mm. In (a), the dotted lines represent the undisturbed trajectories, and the solid lines the trajectories computed with the influence of turbulence on the drop movement. The direction of the flow is from left to right.

sume that all drops crossing a cell of the original grid will cross the corresponding cell of the transformed grid, the partial efficiency of the gauge could be evaluated as a ratio of the sum of the transformed grid cell areas overlapping the gauge orifice to the orifice area of the gauge.

The initial condition was that the drop entered the domain with the horizontal velocity component equal to the free-stream velocity of the air v_f and with the vertical component equal to its terminal velocity w_T, modified by the free-stream turbulence of computed flow fields (Fig. 7). The initial time step Δt was chosen to correspond to the distance of 3 mm divided by the drop initial velocity. Refinements of Δt were necessary near the gauge body in order to achieve a higher precision of the computation. The sizes of the cells of the original grid were between 1.5 mm $\times$ 1.5 mm for the smaller drops and 2.5 mm $\times$ 2.5 mm for the larger drops.

Examples of computed water drop trajectories in the plane of symmetry and the transformed grid in the horizontal plane at the height of the gauge orifice are shown in Fig. 9. In this particular case, the drops passing the turbulent shear layer just behind the windward rim of the gauge orifice are shifted by the stream in the direction of flow, while the drops in front of the gauge arrive at the outer gauge surface. This sudden change in drop trajectories appears as a discontinuity in the transformed grid. For larger drops, the discontinuity disappears and the cells of the transformed grid show only deformations. For smaller drops, the discontinuity eventually stretches over the whole gauge orifice, resulting in zero efficiency of the gauge.

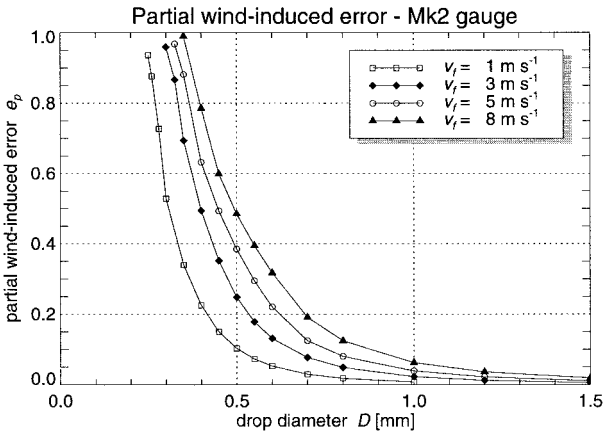

FIG. 10. An example of computed partial wind-induced errors for the Mk2 precipitation gauge.

Figure 10 shows an example of computed partial wind-induced errors for the Mk2 precipitation gauge and different free-stream velocities. The partial wind-induced errors e_p are plotted as a function of drop diameter D. The values of e_p rise with increasing free-stream velocities v_f and decreasing drop diameters D. It is also evident that for drop diameters below a certain limit, D_1, the partial efficiency of the gauge is zero. This limit is a function of the free-stream velocity as well.

e. Estimation of the integral wind-induced error

The integration of the partial error e_p over a drop size distribution results in the integral wind-induced error

TABLE 3. Coefficients in (18) for stagnant air and turbulence, characterized by the turbulent kinematic viscosity $\nu_t = \nu_a$.

Turbulence	Coefficient		
	α_1	α_2	α_3
No	6855.1	1.0525	208.84
Yes	8677.5	1.1213	158.09

TABLE 4. Approximate ranges of the parameter κ for different types of rain, according to Ulbrich (1983).

Type of rain	κ
Orographic rain	$-2 < \kappa < 0$
Thunderstorm rain	$0 < \kappa < 2$
Widespread or stratiform rain	$-1 < \kappa < 5$
Showers	$-4 < \kappa < 5$
Typical range	$-1 < \kappa < 1$

e_i, which is a function of the free-stream velocity, rainfall rate, and drop size distribution. As these parameters vary in time, the integral error is also dependent on time. The integral error e_i can be written as a ratio

$$e_i = \frac{R^*}{R}, \tag{15}$$

where R^* is the total rate of rainfall that is missed by the gauge due to wind action and R is the true rainfall. The true rainfall R [mm h^{-1}] can be expressed as (e.g., Ulbrich 1983)

$$R = C_R \int_{D_{\min}}^{D_{\max}} n_D V_D w_T \, dD, \tag{16}$$

where $C_R = 3.6 \times 10^6$ mm h^{-1} m^{-1} s is the factor for the conversion of the rate of rainfall from [m s^{-1}] to [mm h^{-1}]; n_D [m^{-3} m^{-1}] is the number of drops per unit volume of air and unit drop size interval, with the equivolume spherical diameter D [m] ($D_{\min} \le D \le D_{\max}$); V_D [m^3] is the drop volume; and w_T [m s^{-1}] is the drop terminal velocity. The total missing rate of rainfall R^* [mm h^{-1}] is

$$R^* = C_R \int_{D_{\min}}^{D_{\max}} e_p n_D V_D w_T \, dD, \tag{17}$$

where e_p is the partial wind-induced error.

The lower and upper limits of integration in the above equations can be chosen as $D_{\min} = 0$ and $D_{\max} = \infty$, respectively. Setting these limits leads to an error of integration that, according to Ulbrich (1983), is negligible under certain conditions. Since these conditions are met in most meteorological situations, we used the same assumption about the limits of integration in the present work.

For the computations of the integral wind-induced error, we selected the gamma drop size distribution (Ulbrich 1983) that accounts for the type of rain (e.g., thunderstorm, orographic rain). If, in addition, the partial wind-induced error e_p and drop terminal velocity w_T are approximated by gamma-type functions, they allow an easy integration of (16) and (17).

Thus, terminal velocities of water drops w_T [m s^{-1}] can be expressed as

$$w_T = \alpha_1 D^{\alpha_2} e^{-\alpha_3 D}, \tag{18}$$

where D [m] is the drop diameter, and α_1, α_2, and α_3 are coefficients. In the present computations, the coefficients α_1, α_2, and α_3 were obtained from the nonlinear least squares fit of drop terminal velocities using the Levenberg–Marquardt method (Press et al. 1989). The terminal velocities were computed for the air properties in Table 2 from the approximating formulas by Beard (1977) and then were modified by turbulence, characterized by the turbulent kinematic viscosity $\nu_t = \nu_a$ (see Fig. 7). The resulting coefficients and the coefficients for the case without turbulence are summarized in Table 3.

The gamma drop size distribution n_D [m^{-3} m^{-1}] can be written as

$$n_D = n_0 D^{\kappa} e^{-\Lambda D}, \tag{19}$$

where D [m] is the drop diameter and the parameter κ depends on the type of rain (Ulbrich 1983). Approximate values of κ are given in Table 4. In the above equation, the parameter n_0 [m^{-3} m$^{-\kappa-1}$] is given by the following empirical formula:

$$n_0 = 6 \times 10^{2\kappa+6} e^{3.2\kappa}. \tag{20}$$

An expression for the parameter Λ [m^{-1}] can be derived by substituting (18) and (19) into (16). For the drop volume $V_D = (1/6)\pi D^3$, the result after integration is

$$\Lambda = \left[C_R \frac{\pi}{6} \alpha_1 \frac{n_0}{R} \Gamma(p_1) \right]^{1/p_1} - \alpha_3, \tag{21}$$

where $\Gamma(\cdot)$ is the complete gamma function and the parameter p_1 is

$$p_1 = \alpha_2 + \kappa + 4 > 0. \tag{22}$$

The rate of rainfall R_D [mm h^{-1}], formed by the drop diameters $0 \le D \le D_0$, is

$$R_D = C_R \frac{\pi}{6} \int_0^{D_0} n_D D^3 w_T \, dD. \tag{23}$$

The corresponding fraction of the total volume of incident rainfall can be expressed as

$$E_D = \frac{R_D}{R} = \frac{\gamma(p_1, p_2 D_0)}{\Gamma(p_1)}, \tag{24}$$

which can be obtained by integrating (16) and (23). In the previous equation, $\gamma(\cdot,\cdot)$ is the incomplete gamma function, and the parameter p_2 is

$$p_2 = \alpha_3 + \Lambda. \tag{25}$$

The fraction of the total volume of incident rainfall

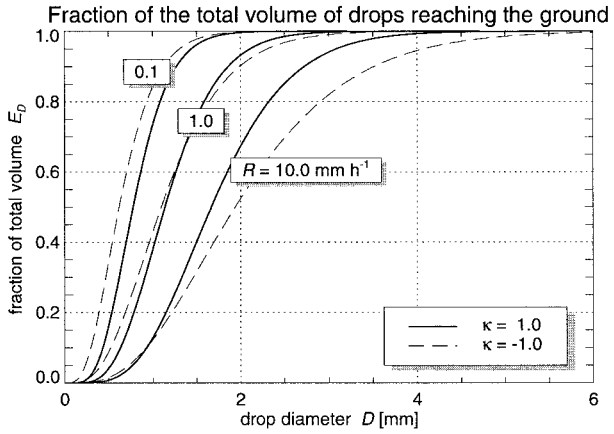

FIG. 11. Fraction of the total volume of drops reaching the ground as a function of drop diameter for the rate of rainfall 0.1, 1.0, and 10.0 mm h^{-1} and for the parameter $\kappa = -1$ and 1. The parameter Λ was evaluated using coefficients α_1, α_2, and α_3 for the case without turbulence (see Table 3).

E_D can be used to illustrate the influence of the type and rate of rainfall on the drop size distribution. Figure 11 shows that the volumetric fraction of smaller drops grows with a decreasing rainfall rate. Except for higher rainfall rates ($R > 10$ mm h^{-1}), the volume fraction of drops with diameters less than 1 mm is larger for orographic rains ($\kappa = -1$) than for thunderstorms ($\kappa = 1$). As is shown in Fig. 10, drops with diameters below 1 mm have the largest partial wind-induced error. Therefore, it can be expected that the integral wind-induced error will be larger for smaller values of parameter κ and smaller rainfall rates R.

For the integration of (17), it is convenient to approximate the partial wind-induced error e_p by a gamma-type function. Similar to formula (18) for the terminal velocities, the approximation can be written as

$$e_p = 1.0, \qquad 0 < D \le D_1,$$
$$e_p = \beta_1 D^{\beta_2} \exp(-\beta_3 D), \qquad D_1 < D < \infty, \tag{26}$$

where β_1, β_2, and β_3 are coefficients, and D_1 [m] is the limit drop diameter. Drops with diameters smaller than D_1 are all blown away from the gauge orifice, resulting in zero efficiency of the gauge.

For a particular gauge and a given free-stream velocity, the values of β_1, β_2, and β_3 in (26) were obtained again by the nonlinear least squares fit of the computed values of the partial wind-induced error for different drop diameters. The analysis of the results indicated that the following relationship is valid:

$$\ln\beta_1 = c_{11}\beta_2 + c_{12}, \tag{27}$$

where c_{11} and c_{12} are further coefficients. Finding coefficients c_{11} and c_{12} removes one degree of freedom in (26) and thus fixes the relationship between β_1 and β_2. The modified version of (26) is then

TABLE 5. Coefficients in (27), (29), (30), and (31) for the determination of parameters β_1, β_2, and β_3.

Coefficient	Type of precipitation gauge		
	Mk2	Hellmann	ASTA
a	-1.1338×10^{-3}	-2.7856×10^{-1}	-1.4493×10^{-1}
b_1	8.7065×10^{-1}	2.0770	1.6347
b_2	−2.7530	−8.9006	−6.3311
c_{11}	8.7834	8.4033	8.2876
c_{12}	2.0191	1.4211	1.5508
c_{21}	2.3871×10^{3}	7.0668	9.3506
c_{22}	1.7604×10^{-1}	-6.4070×10^{-2}	2.8745×10^{-2}
c_{23}	-2.3866×10^{3}	−5.3865	−8.5311
c_{24}	1.6315	1.1367	6.1142×10^{-1}
c_{31}	6.2548×10^{6}	1.9236×10^{4}	2.6959×10^{4}
c_{32}	4.4703×10^{2}	-6.4196×10^{1}	9.5691×10^{1}
c_{33}	-6.2459×10^{6}	-9.3633×10^{3}	-1.8799×10^{4}
c_{34}	3.1218×10^{3}	1.7139×10^{3}	7.4415×10^{2}

$$e_p = 1.0, \qquad 0 < D \le D_1,$$
$$e_p = D^{\beta_2} \exp(c_{11}\beta_2 + c_{12} - \beta_3 D), \qquad D_1 < D < \infty. \tag{28}$$

In comparison with the computation of the wind-induced error without the influence of turbulence on particle movement (Nešpor 1996), the coefficients β_2 and β_3 do not decrease smoothly with increasing free-stream velocity in the present case. Instead, a sudden increase of their values occurs between velocities approximately 2 and 5 m s^{-1}. This can be explained by different effects contributing to the partial error. For example, for lower velocities, certain drop diameters, after penetrating the gauge through the shear layer, are captured by the inner vortex and circulated, and some may escape the gauge. This effect is suppressed in the case of larger velocities in which the partial wind-induced error is caused only by the windward shift of the drops in the turbulent shear layer. The drops penetrating into the gauge are large enough not to circulate in the inner vortex, and they are caught by the gauge.

The analysis of the results revealed that for all of the investigated gauges the following functions can be used:

$$\beta_2 = c_{21}v_f^a + c_{22}v_f + c_{23} + c_{24}y \tag{29}$$

and

$$\beta_3 = c_{31}v_f^a + c_{32}v_f + c_{33} + c_{44}y, \tag{30}$$

where y is the function representing the sudden increase in values of β_2 and β_3. It can be approximated by

$$y = \arctan(b_1 v_f + b_2). \tag{31}$$

The values of the exponent a and coefficients b_1, b_2, $c_{21}, \ldots, c_{24}$, $c_{31}, \ldots, c_{34}$ in the above approximating equations were obtained by the nonlinear least squares fit and are summarized in Table 5.

Using the integration limits $D_{\min} = 0$ and $D_{\max} = \infty$, and the limit diameter D_1, (17) can be rewritten in the form

$$R^* = C_R\left(\int_0^\infty e_p n_D V_D w_T \, dD - \int_0^D (e_p - 1) n_D V_D w_T \, dD\right). \tag{32}$$

The substitution of the drop volume $V_D = (1/6)\pi D^3$, the substitution of (18), (19), and (26) into (32), and the subsequent integration gives the total missing rate of rainfall in the form

$$R^* = C_R \frac{\pi}{6} n_0 \alpha_1 \times \left\{\frac{1}{p_2^{p_1}}\gamma(p_1, p_2 D_1) + \frac{\beta_1}{p_4^{p_3}}[\Gamma(p_3) - \gamma(p_3, p_4 D_1)]\right\}, \tag{33}$$

where parameters p_1 and p_2 are defined by formulas (22) and (25), respectively, and parameters p_3 and p_4 are

$$p_3 = p_1 + \beta_2 > 0 \tag{34}$$

and

$$p_4 = p_2 + \beta_3. \tag{35}$$

In (33), the incomplete and complete gamma functions can be evaluated from known arguments using approximating formulas (e.g., Press et al. 1989).

Equation (26) for $D = D_1$ ($e_p = 1$) can be rewritten as

$$D_{1,i+1} = \frac{1}{\beta_3}\ln(\beta_1 D_{1,i}^{\beta_2}), \tag{36}$$

where i is the iteration number. The limit diameter can be iteratively computed from (36) starting from $D_{1,0} = 0.0005$ m.

3. Results

We used the above procedure to evaluate the integral wind-induced error of investigated precipitation gauges as a function of rainfall rate R and to estimate differences between gauges. For the evaluation, we selected drop size distribution parameters $\kappa = -1$ and 1, and two groups of wind velocities: $v_f = 1$ and 3 m s^{-1} and $v_f = 5$, 10, and 15 m s^{-1}. The parameter $\kappa = -1$ is on the lower boundary of the typical range, and it can be regarded as a value representing an orographic rain. On the other hand, the parameter $\kappa = 1$ is on the upper boundary of the typical range, and it corresponds to a thunderstorm rain (Table 4). For lower rainfall rates ($R < 10$ mm h^{-1}), a rainfall characterized by $\kappa = -1$ is composed of a larger portion of smaller drops ($D < 1$ mm) than a rainfall characterized by $\kappa = 1$ (Fig. 11).

The results for lower wind speeds in Fig. 12 show that the integral wind-induced error grows with a decreasing rate of rainfall. The increase is relatively small for rainfall rates above 2 mm h^{-1} but large for rates below 1 mm h^{-1}. In Fig. 13, a similar tendency can be also observed for higher wind speeds. This results from a larger volumetric fraction of smaller drops in rains with lower rates compared to rains with higher rates, as illustrated in Fig. 11.

The integral wind-induced error also depends on the

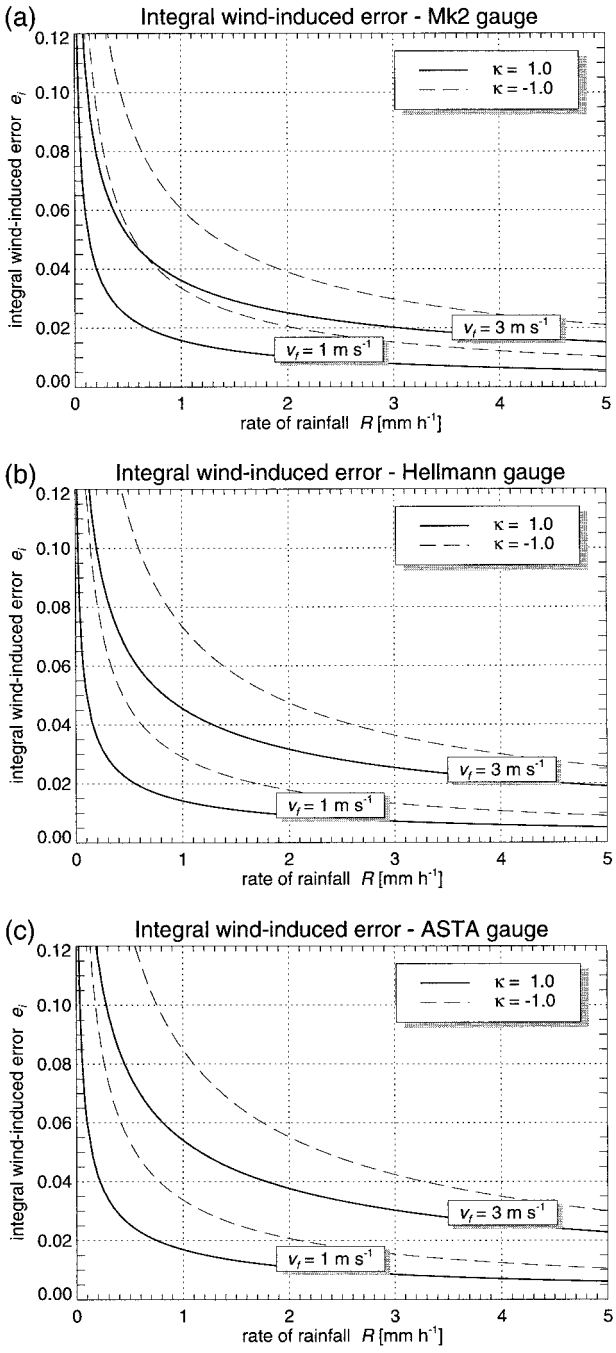

FIG. 12. The integral wind-induced error e_i of (a) the Mk2, (b) Hellmann, and (c) ASTA precipitation gauges is plotted as a function of the rate of rainfall R. The error was computed for the free-stream velocities $v_f = 1$ and 3 m s^{-1} (labels in the plot) and for the gamma drop size distribution parameters $\kappa = -1$ (orographic rains) and $\kappa = 1$ (thunderstorm rains).

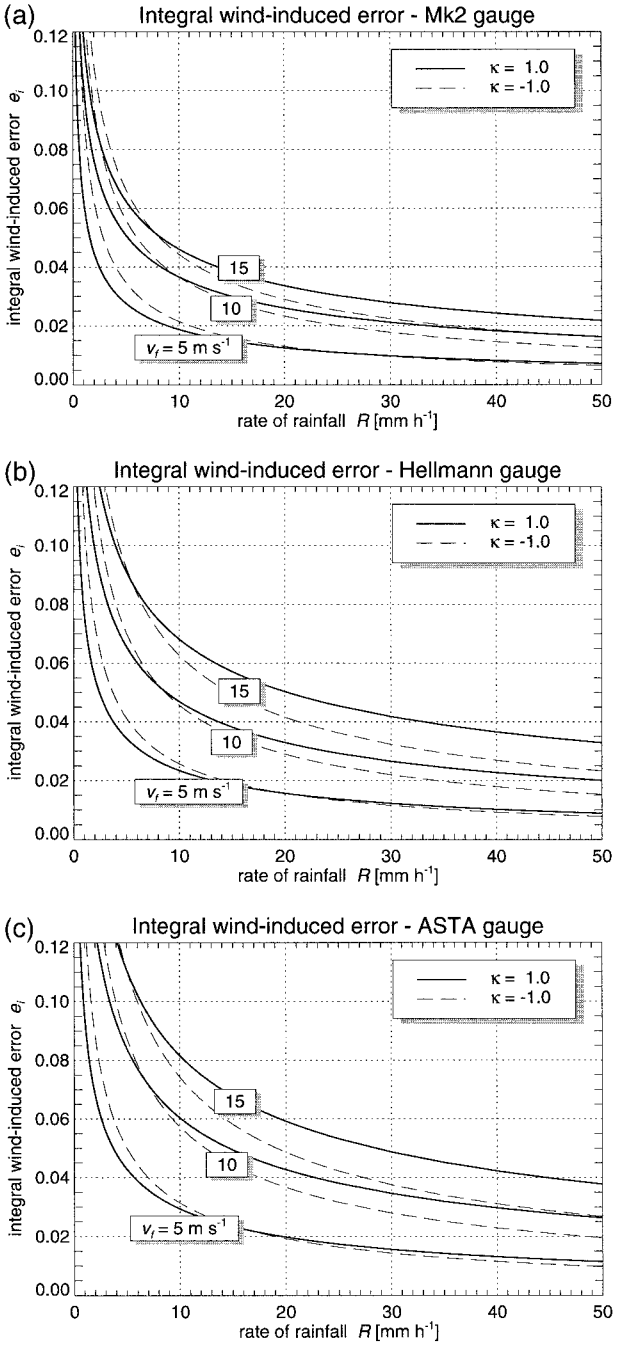

FIG. 13. The same as Fig. 12 but for the free-stream velocities v_f = 5, 10, and 15 m s^{-1}. Note the different scale of the rainfall-rate axis.

type of rainfall. For the same rainfall rate in the lower range ($R < 5$ mm h^{-1}), a rainfall with a larger volumetric fraction of drops smaller than 1 mm ($\kappa = -1$) shows a larger error than a rainfall with a smaller fraction ($\kappa = 1$). This effect is emphasized with a decreasing rate of rainfall. For example, in the case of the Hellmann gauge, wind velocity of 3 m s^{-1}, and rate of rainfall of 1 mm h^{-1}, the integral wind-induced error is 7.3% for orographic rains ($\kappa = -1$) and 4.6% for thunderstorm rains ($\kappa = 1$) (see Fig. 12b).

The influence of parameter κ is reversed for higher rainfall rates ($R \geq 10$ mm h^{-1}) and wind speeds ($v_f \geq 10$ m s^{-1}). In this case, rains with a smaller parameter κ show lower errors than those with a larger κ (Fig. 13). This can be explained by an increase in the fraction of drop diameters between 1 and 2 mm in the total rain volume, as shown in Fig. 11 for $R = 10$ mm h^{-1}.

The wind velocity also has a significant influence on the magnitude of the integral wind-induced error and, as expected, the error increases with increasing wind velocity. In general, the error is larger for lower values of rainfall rate and higher wind velocities.

In addition, there are differences between investigated precipitation gauges. The results reveal that, of all of the gauges, the ASTA gauge has the largest wind-induced error and the Mk2 has the smallest wind-induced error. For example, for $R = 1$ mm h^{-1}, $v_f = 3$ m s^{-1}, and $\kappa = 1$, the integral wind-induced error is 3.6%, 4.6%, and 5.3% for the Mk2, Hellmann, and ASTA gauges, respectively (see Fig. 12). The only exceptions are the wind velocities below approximately 1.5 m s^{-1}. For those low velocities, the Hellmann gauge shows slightly smaller errors than the Mk2 gauge. A similar qualitative difference between the Hellmann and ASTA gauges was observed in field measurements (Sevruk 1989a).

4. Comparison with field measurements

During a real rainfall event, the input parameters (the wind speed, rainfall rate, and drop size distribution parameter) change their values with time. The correct approach to estimate the time-averaged wind-induced error by the present procedure would be to base the computation on high temporal resolution measurements of input parameters and to evaluate the error for each time step. This is practically impossible, as the high temporal resolution data are very rarely available. If we suppose that the dependence of the error on input parameters is locally linear, it is possible to base error computations on time-averaged values of input parameters.

The present comparison of computational results and field measurements of the wind-induced error of rainfall in Fig. 14 is based on the study of Sevruk (1989b). In this study, the wind-induced error was estimated from comparison measurements of paired elevated (1.5 m above ground) and ground-level Hellmann precipitation gauges. The estimates were based on 10 years of measurements during the summer half-year (April–September). The measurements had been carried out in Les Avants, Switzerland (1000 m MSL), from 1938 to 1947. The mean rates of rainfall were estimated on a daily basis from precipitation sums of the elevated gauge divided by the precipitation durations. The mean wind speeds at the gauge orifice height were assessed by reducing the values measured at the height of 10 m using

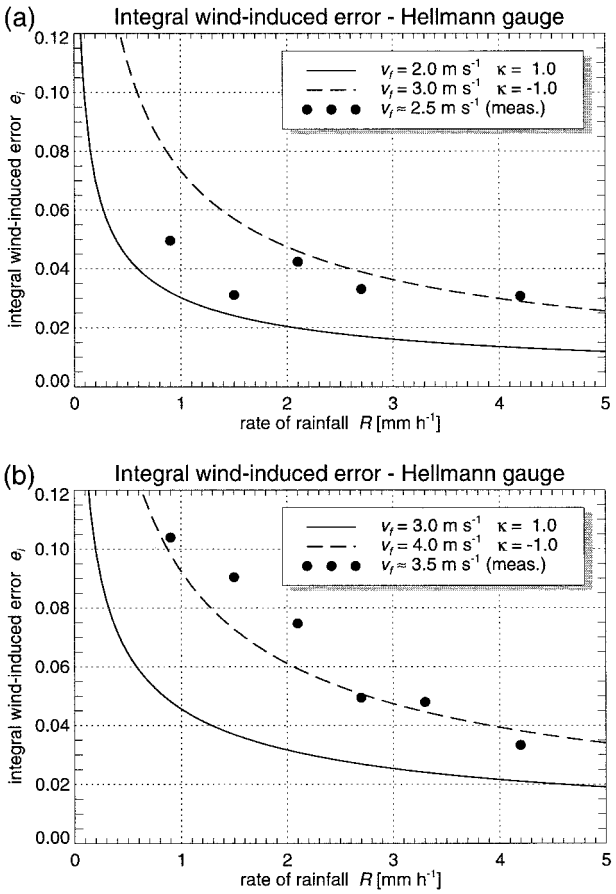

FIG. 14. Comparison of the computed integral wind-induced error e_i with values estimated from measurements (Sevruk 1989b). The measured values (points) are rainfall-rate class averages of several rainfall events for (a) wind velocities between 2 and 3 m s^{-1} and (b) between 3 and 4 m s^{-1}. The curves represent computed errors for the upper boundaries of wind speed classes and parameter $\kappa = -1$ (dashed lines) and for the lower boundaries of wind speed classes and parameter $\kappa = 1$ (solid lines).

a logarithmic wind profile. There was no information about the drop size distributions.

To eliminate random errors of measurement, the data were subdivided into classes according to the mean rainfall rate and wind speed at the gauge orifice height (see Sevruk 1989b). In the present comparison, the error is expressed as the ratio of the difference between the ground-level and the elevated gauge rainfall amounts to the ground amount. In Fig. 14, the estimated wind-induced errors are plotted for different class averages of rainfall rates and for two classes of wind speed: between 2 and 3 m s^{-1} and between 3 and 4 m s^{-1}. They are compared to values that are estimated by using present numerical simulations. We computed the wind-induced error for the upper boundaries of wind speed classes and drop size distribution parameter $\kappa = -1$ (dashed lines in Fig. 14) and for the lower boundaries of wind speed classes and parameter $\kappa = 1$ (solid lines in Fig. 14). Although there are many uncertainties in measurements and simplifications in numerical simulations, the errors estimated from measurements agree quite well with present computations.

5. Conclusions

The presented numerical simulation proved to be capable of estimating the wind-induced error of rainfall measurements by various precipitation gauges. As expected, there are differences between gauges. Generally, the larger the blockage of the airflow by the gauge body, the higher is the error. The error is also larger for rains with larger fractions of smaller drops and for higher wind speeds.

Although the computed wind-induced error estimates seem to be quite realistic, further improvements of the computational procedure are possible. First, the present approximation of the influence of turbulence on particle movement is limited to the computed flow fields characterized by low free-flow turbulence. An application of another approximation would probably require a deeper study of particle movement in turbulent flow fields. It would also be possible to improve the computation of the flow around precipitation gauges, by modifying the vertically uniform boundary conditions or by employing more sophisticated turbulence model, for example.

The formulas, derived from the numerical simulation, can be used for the direct correction of measured precipitation amounts if the wind speed, rate of rainfall, and drop size distribution are measured with a high temporal resolution. This is usually not the case, and quite often only the rate of rainfall is measured. Therefore, the present formulas can be used to check old correction procedures and to develop new correction procedures based on estimates and averages of input parameters. To reach this goal, further investigations on time-dependent wind speed, rainfall rate, and drop size distribution for individual rainfall events are necessary.

Further, the numerical simulation could be applied to checking the performance of various precipitation gauges and gauges equipped with wind shields. These investigations would provide a better understanding of the influence of different shape parameters of the gauge. They could result in shape improvements and, possibly, in a design of a new precipitation gauge with reduced wind-induced error. (Note: The final formulas for computing the integral wind-induced error for the Mk2, Hellmann, and ASTA precipitation gauges were built into subroutines that correct the measured rainfall rate for known wind speed and drop size distribution. The subroutines are coded in C, and they can be obtained via e-mail from the author.)

In the present work the numerical simulation of the airflow and particle movement was used to estimate the wind-induced error of rainfall measurements, but the same procedure is applicable to snowfall as well. In this case, the difference will be in the size distribution and

terminal velocities of snow particles, which, compared to raindrops, have a much larger variety of shapes and densities.

Acknowledgments. The present work was supported by the Swiss National Foundation for Scientific Research in Bern (Project 20-5053.86), and partially by the Swiss Federal Institute of Technology and the Swiss Meteorological Institute in Zurich. The wind tunnel measurements were made in cooperation with the Institute of Hydromechanics and Water Resources Management of the Swiss Federal Institute of Technology, Zurich.

REFERENCES

Astrup, P., 1992: Turbulent gas-particle flow. Technical Rep., Risø-R-618(EN), Risø National Laboratory, Roskilde, Denmark, 133 pp. [Available from Risø Library, Risø National Library, P.O. Box 49, DK-4000, Roskilde, Denmark.]

Beard, K. V., 1976: Terminal velocity and shape of cloud and precipitation drops aloft. *J. Atmos. Sci.,* **33,** 851–864.

——, 1977: Terminal velocity adjustment for cloud and precipitation drops aloft. *J. Atmos. Sci.,* **34,** 1293–1298.

Carlsson, B., and U. Svensson, 1984: Wind correction factors for snow precipitation gauges. *Proc. 5th Research Basin Symp.,* Helsinki, Finland, Finnish Meteorological Institute, 1.15–1.30.

Folland, C. K., 1988: Numerical models of the rain-gauge exposure problem, field experiments, and an improved collector design. *Quart. J. Roy. Meteor. Soc.,* **114,** 1485–1516.

Gunn, R., and G. D. Kinzer, 1949: The terminal velocity of fall for water drops in stagnant air. *J. Meteor.,* **6,** 243–248.

Hall, D. J., J. G. Irwin, B. H. Stone, and S. L. Upton, 1993: Aerodynamic considerations in precipitation collector design. *Measurement of Airborne Pollutants,* S. Couling, Ed., Butterworth-Heinemann, 108–148.

Hinze, J. O., 1975: *Turbulence.* McGraw-Hill, 790 pp.

Launder, B. E., and D. B. Spalding, 1974: The numerical computation of turbulent flows. *Comput. Methods Appl. Mech. Eng.,* **3,** 269–289.

Lomas, C. G., 1986: *Fundamentals of Hot Wire Anemometry.* Cambridge University Press, 211 pp.

Narasimhamurty, G. S. R., A. Purushothaman, and K. Sivaji, 1986: Hydrodynamics of liquid drops in air. *Gas-Liquid Flows,* N. P. Cheremisinoff, Ed., Vol. 3, Gulf Publishing, 43–57.

Nešpor, V., 1996: Investigation of wind-induced error of precipitation measurements using a three-dimensional numerical simulation. Zürcher Geographische Sehriften 63, 117 pp. [Available from Department of Geography, Swiss Federal Institute of Technology (ETH), Winterthurerstr. 190, 8057 Zurich, Switzerland.]

Press, W. H., B. P. Flannery, S. A. Teukolsky, and W. T. Vetterling, 1989: *Numerical Recipes.* Cambridge University Press, 702 pp.

Sevruk, B., 1985: Correction of precipitation measurements. *Proc. Workshop on the Correction of Precipitation Measurements,* Zurich, Switzerland, WMO/IAHS/ETH, 13–23.

——, 1989a: Reliability of precipitation measurement. Proc. International Workshop on Precipitation Measurement, WMO Tech. Document 328, 13–19. [Available online at http://www.wmo.ch.]

——, 1989b: Wind induced measurement error for high-intensity rains. Proc. International Workshop on Precipitation Measurement, WMO Tech. Document 328, 199–204. [Available online at http://www.wmo.ch.]

——, and W. R. Hamon, 1984: International comparison of national precipitation gauges with a reference pit gauge. Instruments and Observing Methods Rep. 17, WMO, Geneva, Switzerland, 86 pp. [Available online at http://www.wmo.ch.]

Stout, J. E., S. P. Atya, and E. L. Genikhovich, 1995: The effect of nonlinear drag on the motion and settling velocity of heavy particles. *J. Atmos. Sci.,* **52,** 3836–3848.

Ulbrich, C. W., 1983: Natural variation in the analytical form of the raindrop size distribution. *J. Climate Appl. Meteor.,* **22,** 1764–1775.

Yang, D., B. Sevruk, E. Elomaa, V. Golubev, B. Goodison, and T. Günther, 1994: Wind-Induced Error of Snow Measurement: WMO Intercomparison Results. *Proc. 23d Int. Tagung für Alpine Meteorologie,* Lindau, Germany, Annalen der Meteorologie 30, 61–64.